Title

Systematic Underestimation of Canopy Conductance Sensitivity to Drought by Earth System Models

Journal

AGU Advances, 5(1)

ISSN

2576-604X

Authors

Green, JK

Zhang, Y

Luo, X

et al.

Publication Date

2024-02-01

DOI

10.1029/2023av001026

AGU ADVANCING EARTH AND SPACE SCIENCES

AGU Advances

RESEARCH ARTICLE
10.1029/2023AV001026

Systematic Underestimation of Canopy Conductance Sensitivity to Drought by Earth System Models

J. K. Green[1,2], Y. Zhang[3], X. Luo[4,5], and T. F. Keenan[2,6]

[1]Department of Environmental Science, University of Arizona, Tucson, AZ, USA, [2]Department of Environmental Science, Policy, and Management, University of California, Berkeley, Berkeley, CA, USA, [3]Sino-French Institute for Earth System Science, College of Urban and Environmental Sciences, Peking University, Beijing, China, [4]Department of Geography, National University of Singapore, Singapore, Singapore, [5]Center for Nature-based Climate Solutions, National University of Singapore, Singapore, Singapore, [6]Climate and Ecosystem Sciences Division, Lawrence Berkeley National Laboratory, Berkeley, CA, USA

Peer Review The peer review history for this article is available as a PDF in the Supporting Information.

Key Points:

- Earth System Models (ESMs) underestimate the sensitivity of canopy conductance to changes in moisture availability
- The underestimation is greatest in semi-arid and bordering regions with temperatures between 5 and 25°C and leaf area index over 1
- This misrepresentation leads to errors in ESM projections of carbon, water, and energy fluxes during drought

Supporting Information:

Supporting Information may be found in the online version of this article.

Correspondence to:

J. K. Green and T. F. Keenan,
juliakgreen@arizona.edu;
trevorkeenan@berkeley.edu

Citation:

Green, J. K., Zhang, Y., Luo, X., & Keenan, T. F. (2024). Systematic underestimation of canopy conductance sensitivity to drought by Earth System Models. *AGU Advances*, *5*, e2023AV001026. https://doi.org/10.1029/2023AV001026

Received 3 AUG 2023
Accepted 25 NOV 2023

Author Contributions:

Conceptualization: J. K. Green, T. F. Keenan
Formal analysis: J. K. Green
Investigation: J. K. Green
Methodology: J. K. Green, Y. Zhang, X. Luo, T. F. Keenan
Supervision: T. F. Keenan
Validation: J. K. Green
Writing – original draft: J. K. Green

Abstract

The response of vegetation canopy conductance (g_c) to changes in moisture availability (γ_{gc}^m) is a major source of uncertainty in climate projections. While vegetation typically reduces stomatal conductance during drought, accurately modeling how and to what degree stomata respond to changes in moisture availability at global scales is particularly challenging, because no global scale g_c observations exist. Here, we leverage a collection of satellite, reanalysis and station-based near-surface air and surface temperature estimates, which are physically and statistically linked to γ_{gc}^m due to the local cooling effect of g_c through transpiration, to develop a novel emergent constraint of γ_{gc}^m in an ensemble of Earth System Models (ESMs). We find that ESMs systematically underestimate γ_{gc}^m by ~33%, particularly in grasslands, croplands, and savannas in semi-arid and bordering regions of the Central United States, Central Europe, Southeastern South America, Southern Africa, Eastern Australia, and parts of East Asia. We show that this underestimation occurs because ESMs inadequately reduce g_c when soil moisture decreases. As g_c controls carbon, water and energy fluxes, the misrepresentation of modeled γ_{gc}^m contributes to biases in ESM projections of gross primary production, transpiration, and temperature during droughts. Our results suggest that the severity and duration of droughts may be misrepresented in ESMs due to the impact of sustained g_c on both soil moisture dynamics and the biosphere-atmosphere feedbacks that affect local temperatures and regional weather patterns.

Plain Language Summary

During photosynthesis, plants open their stomata to take in carbon dioxide and inevitably, lose water through transpiration. As a result, when soil moisture is low, plants reduce their stomatal apertures to conserve water, simultaneously reducing their carbon dioxide uptake. It is critical for Earth System Models (ESMs) to incorporate accurate vegetation responses to moisture availability to make accurate future climate projections. Here, we show that these ESMs are systematically underestimating the sensitivity of vegetation to moisture availability, and that this underestimation is leading to incorrect climate projections of carbon, water, and energy fluxes during droughts.

1. Introduction

Stomatal conductance regulates and couples the exchange of carbon, water, and energy fluxes between the atmosphere and terrestrial biosphere (Berry et al., 2010). When environmental conditions are not limiting for photosynthesis and transpiration, plants open their stomata to maximize the uptake of atmospheric carbon dioxide while regulating the transport of water between the ground and the atmosphere. However, when environmental conditions are limiting (e.g., when water supply drops below a critical threshold), plants tend to reduce stomatal aperture and can experience leaf senescence (reducing leaf area index; LAI), generally leading to lower rates of carbon uptake (i.e., gross primary production [GPP]) and transpiration (Buckley, 2019). The surface energy budget then shifts toward less latent heat (LE), and more sensible heat (H) is emitted to the atmosphere, amplifying atmospheric dryness and temperature (Humphrey et al., 2021). As a result, canopy conductance, the sum of stomatal conductance integrated through all leaves within a canopy (g_c), exerts a strong biophysical feedback on the climate system. In the long term, g_c impacts the climate by mediating the rate of removal of CO_2 from the atmosphere by plants (Friedlingstein et al., 2022). In the short-term, g_c can alter cloud coverage and rainfall patterns through biosphere-atmosphere feedbacks (Forzieri et al., 2020; Green et al., 2017). Canopy conductance is therefore an essential component of Earth System Models (ESMs), and thus future climate projections.

Writing – review & editing: J. K. Green, Y. Zhang, X. Luo, T. F. Keenan

While it is essential to include an accurate representation of g_c and its feedbacks in ESMs to obtain robust climate projections, doing so is hindered by a lack of adequate theory. Specifically, how stomata respond to atmospheric dryness and moisture anomalies, and the exact mechanisms that drive the response remain elusive (Buckley, 2019). For this reason, representing g_c mechanistically in ESMs has been challenging, resulting in a diversity of approaches. Semi-empirical approaches derived from leaf level measurements (Ball et al., 1987; Leuning, 1995) are widely used, but were created based on well-watered conditions, and require the sensitivity of g_c to soil moisture to be parameterized. This parameterization makes it difficult to capture the wide range of variability in stomatal responses to dryness across species or varying canopy heights (Sabot et al., 2022), and has led to less accurate g_c predictions during periods of soil moisture stress (G. B. Bonan et al., 2014). On the other hand, there are optimization-based process implementations (Farquhar & Cowan, 1977; Medlyn et al., 2011), based on the idea that g_c optimizes plant carbon gain per water lost. However, these approaches also rely on empirical moisture stress factors to downregulate stomatal conductance during periods of low moisture supply (Sabot et al., 2022), also resulting in greater uncertainty in low soil moisture conditions. The optimization-based models have not necessarily outperformed the semi-empirical ones (Franks et al., 2018).

The implementation of realistic processes for simulating g_c is further complicated by the paucity of observations at spatial scales relevant to ESM projections. Most available measurements are at the leaf-scale (Buckley, 2019; Vicente-serrano et al., 2022), because it is not currently possible to observe g_c and its sensitivity to moisture availability at regional or global scales. And while it *is* possible to scale stomatal conductance somewhat accurately to the canopy scale using big-leaf assumptions (Baldocchi et al., 1991; Bonan et al., 2021), due to heterogeneity in topography, varying ecosystem traits, and climactic conditions, scaling these measurements up to evaluate the sensitivity of g_c to moisture availability (γ^m_{gc}) in ESMs has not yet been feasible. This has resulted in the absence of an observational benchmark to guide the ESM representation of γ^m_{gc} and additionally hinders our ability to evaluate it. As a result, the response of vegetation to moisture availability has emerged as a major source of uncertainty in carbon cycle and climate projections (Trugman et al., 2018).

Here we develop and implement a method to assess the representation of canopy conductance responses to deficits in moisture (represented by the Standardized Precipitation Evaporation Index [SPEI]) in ESMs, despite the lack of direct observations of it. This is done by exploiting heuristic relationships between γ^m_{gc}, and the sensitivity of the difference between land surface temperature (*LST*) and near surface air temperature (*Tair*) to moisture availability ($\gamma^m_{LST-Tair}$), in the form of an emergent constraint. It is well established that the difference between *LST* and *Tair* can be indicative of vegetation water stress, due to the strong control that g_c can exert on evaporative cooling and thus the surface energy balance, and that satellite measurements of these quantities can be used to gain insight into vegetation status (Farella et al., 2022; Green et al., 2022). Thus, we establish spatially explicit relationships between γ^m_{gc} and $\gamma^m_{LST-Tair}$ across ESM estimates from the Coupled Model Intercomparison Project Phase 6 (CMIP6) (Figures S1–S4 and Table S1 in Supporting Information S1) to identify an emergent constraint (Hall & Qu, 2006; Williamson et al., 2021) on γ^m_{gc}. In doing so, we are able to evaluate the representation of γ^m_{gc} across ESMs by using $\gamma^m_{LST-Tair}$ calculated from observations, and to investigate how the ESM misrepresentation of γ^m_{gc} can lead to incorrect projections of carbon, water, and energy fluxes through biosphere-atmosphere feedbacks.

2. Materials and Methods

2.1. Emergent Constraint Theory

An emergent constraint hinges upon the presence of a strong heuristic relationship between an observable variable (X) and an unobservable variable (Y) that is represented in an ensemble of models (Hall et al., 2019; Williamson et al., 2021). While individual models may have incorrect values for variables X and Y, if the heuristic relationships between them are preserved across the ensemble of models, when examined collectively across them, the consistency of this relationship allows for observational data to be used to constrain the unobservable (modeled) variable Y. The heuristic relation between X and Y should be based on underlying physical principles relating Y to X.

Here, the emergent constraint we developed is based on the physical relationship between g_c, and the partitioning of surface energy fluxes when vegetation is water limited (Monteith, 1965; Penman, 1948). When the Penman-Monteith equation is inverted to solve for g_c (Equation 1), where γ is the psychometric constant, g_a is

the aerodynamic conductance in m/s, *LE* is latent heat flux in W/m^2, Δ is the slope of the saturated vapor pressure curve in kPa/K, R_n is net radiation in W/m^2, *G* is the ground heat flux in W/m^2, ρ is the density of the air in kg/m^3, and c_p is the specific heat of the air, 1,004 J/kg/K, one can see that g_c is directly related to the surface energy balance and *LST-Tair* (Equation 2), where *r* is the compound aerodynamic resistance from the air, soil, and vegetation, and *H* is the sensible heat flux in W/m^2.

$$g_c = \frac{\gamma g_a LE}{\Delta(Rn - G - LE) + \rho c_p g_a VPD - \gamma LE} \quad (1)$$

$$H = Rn - G - LE = \rho c_p \frac{LST - Tair}{r} \quad (2)$$

In other words, when plants are stressed by low water supply or high water demand, they tend to close their stomata to conserve water, thus reducing transpiration and *LE*, increasing *H*, and therefore increasing leaf surface temperature relative to *Tair* (increasing *LST-Tair*). Turbulent fluxes and $g_{c,}$ are modeled with deterministic equations, but the relationship between them in the presence of atmospheric coupling is an emerging property of each ESM. The emergent constraint applied here is based on the fact that although each CMIP6 ESM has a different γ^m_{gc} and $\gamma^m_{LST-Tair}$, each ESM has a physically- and statistically based relationship between γ^m_{gc} and $\gamma^m_{LST-Tair}$ when water is limiting for photosynthesis (Figures S1–S4 in Supporting Information S1). This relationship across the ensemble of ESMs allows us to effectively use information contained in observation-based estimates of $\gamma^m_{LST-Tair}$ to constrain ESM γ^m_{gc} collectively, despite the lack of g_c observations at regional spatial scales (Figures S1–S4 in Supporting Information S1) (Hall et al., 2019). Specifically, the emergent constraint examined how relative changes of growing season g_c (calculated as a deviation from its 90th percentile value: an unstressed value) and anomalies of the difference between *LST* and *Tair* varied with moisture availability over the time period of 2000–2014 (Figure S2 in Supporting Information S1).

While often used to constrain model projections of future climate (Cox et al., 2018; Hall & Qu, 2006; Shiogama et al., 2022), the technique was applied here to constrain ESM representation of environmental processes in the historical simulations, to provide a benchmark for present-day γ^m_{gc}. Emergent constraints also tend to be applied for large regional or global analyses, but we applied it spatially (pixel-by-pixel) to achieve a cohesive understanding of ESM performance across vegetated areas that experience water limitation. Because the physical and statistical relationship between γ^m_{gc} and $\gamma^m_{LST-Tair}$, which is necessary for an emergent constraint, does not exist everywhere (e.g., regions with no water limitation) (Figures S1 and S5 in Supporting Information S1), only those results for regions where these requirements held are included in the analysis.

2.2. ESM Calculations of γ^m_{gc} and $\gamma^m_{LST-Tair}$

Prior to performing the emergent constraint, γ^m_{gc} and $\gamma^m_{LST-Tair}$ had to be calculated per-pixel for each of the 30 CMIP6 ESMs (Table S1 in Supporting Information S1) used in the constraint. We used monthly growing season data from the historical runs for 2000–2014 using consistent ESM forcing data (ESM variant labels listed in Table S1 in Supporting Information S1). Before performing calculations, all ESM data sets were brought to a standard spatial resolution of 288 by 192 grid cells, which matched the finest spatial resolution of the ESMs (e.g., the spatial resolution of CESM2). The growing season was defined as months when the local monthly temperature climatology was greater than 278K, and the monthly net radiation climatology was at least 60% of the maximum monthly climatology value. Following the data processing, growing season estimates of g_c, *LST-Tair* [the difference between the CMIP6 variables skin temperature ("ts") and near surface air temperature ("tas")], and moisture availability were calculated, and were regressed against one another to determine γ^m_{gc} and $\gamma^m_{LST-Tair}$ (Figure S2 in Supporting Information S1).

$$g_c = \frac{T \times P}{VPD} \quad (3)$$

To calculate g_c, Fick's law was used (Equation 1) where *T* is transpiration, *P* is surface pressure, and *VPD* is vapor pressure deficit. *VPD* was calculated based on the Clausius-Clapeyron relationship (Equation 2) where L_v is the latent heat of vapourization, 2.5×10^6 J/kg, R_v is the vapor gas constant, 461 J/K/kg, *Tair* is in units of Kelvin, and relative humidity is expressed as a percentage. This formulation to calculate g_c is typically used at the leaf-level, and

$$VPD = 6.11 * \exp\left[\frac{L_v}{R_v} * \left(\frac{1}{273} - \frac{1}{Tair}\right)\right] * \left(1 - \frac{RH}{100}\right) \quad (4)$$

is not commonly applied at larger spatial scales (Jarvis & Mcnaughton, 1986). This is due to the additional impacts of aerodynamic conductance (g_a) from canopy structure and thus surface roughness, which can make the quantity difficult to interpret as one scales from a leaf to a vegetated canopy. For this reason, inverting the Penman-Monteith equation (Monteith, 1965; Penman, 1948) to obtain surface conductance (Equation 1), would be a more direct way of calculating g_c. To use this equation, the psychometric constant could be calculated according do Equation 5, where $\varepsilon = 0.622$, Δ could be calculated according to Equation 6, where e_s is the saturation vapor pressure in Pa, and g_a could be calculated according to Equation 7, where K is the unitless von Karman constant, 0.4, U is the wind speed at height z in m/s, z_d is the zero plane displacement taken as 2/3 the canopy height in meters, and z_o is the momentum roughness length taken as 1/10 the canopy height in meters (Campbell & Norman, 1998).

$$\gamma = \frac{Pc_p}{\varepsilon L_v} \quad (5)$$

$$\Delta = \frac{L_v e_s}{R_v Tair^2} \quad (6)$$

$$g_a = \frac{K^2 U}{\ln\left(\frac{z - z_d}{z_o}\right)^2} \quad (7)$$

However, there are a limited number of ESMs that output vegetation height data (less than 5), which is a necessary input for calculating g_a (Equation 7).

Thus, due to the small number of ESMs available, we were not able to construct an emergent constraint using the Penman-Monteith inversion method. However, we were able to calculate γ^m_{gc} and γ^m_{ga} for those ESMs that did output vegetation height data, to ensure that using Fick's law to calculate γ^m_{gc} was not skewing the results (Figures S6 and S7 in Supporting Information S1). For this analysis, the ground heat flux, G, was assumed to be negligible, and the wind measurement height was set to 10-m (the typical height in the ESMs) when the vegetation height was below 9-m tall, and when the vegetation height was above 10-m it was estimated to be the mean vegetation height plus 2-m. We found that when we compared the output from the 2 methods (after converting those values to deviations from the 90th percentile value) for the four available ESMs (CESM2, CMCC-ESM2, NorESM2-MM, and UKESM1-0-LL), that the RMSE-values ranged from 3.69% to 3.99% for γ^m_{gc}, while the RMSE-values for comparing γ^m_{ga} from the Penman-Monteith method, and γ^m_{gc} calculated using Fick's Law demonstrated only a weak relationship between them. These results left us confident that our simplified Fick's Law calculation of γ^m_{gc} in the ESMs indeed largely represented changes in g_c rather than changes in γ^m_{ga}.

To represent moisture availability, we used the *SPEI*, a drought index that uses precipitation and potential evaporation data to characterize moisture anomalies. The *SPEI* was used instead of root zone soil moisture data due to the limited number of measurements that coincided with our time period of interest (observational data from 2003 to 2019 was used for our analysis, while for instance, Level 4 Soil Moisture Active Passive data was not available until 2015 and other soil moisture products are based on models with large uncertainties). The *SPEI* was also chosen instead of the Standardized Precipitation Index which takes into account precipitation but not potential evaporation, and has a weaker relationship with g_c and *LST-Tair* than *SPEI* which we determined via correlations.

The *SPEI* was generated using the R package "SPEI" (Beguería & Vicente-Serrano, 2023) using monthly precipitation and temperature data from the historical runs for 1985–2014. The Thornthwaite equation (Thornthwaite, 1948) was used to calculate potential evapotranspiration, and the *SPEI* was calculated based on a log-logistic distribution function and a 12-month timescale. We examined timescales for the *SPEI* between 3- and 12-month and chose to use 12-month for the main analysis, as this resulted in the greatest number of pixels across ESMs having relationships between g_c and *SPEI* with a p-value < 0.1.

To define the sensitivity of ESM g_c and *LST-Tair* to *SPEI* per pixel, the g_c data was converted to a percent deviation from the 90th percentile value (a time-period of no stress), and *LST-Tair* was first converted to anomalies

(the seasonal cycle was removed). These were then linearly regressed against the local *SPEI* data for each pixel location. The sensitivity was taken as the slope of those relationships (Figure S2 in Supporting Information S1). Although this relationship is not truly linear (i.e., when water is not limiting g_c tends to reach a maximum value i.e., maintained when moisture supplies increase further) (Feldman et al., 2018; Fu et al., 2022; Green et al., 2022), should a particular location have data points that reflect the maximum g_c value where there is saturation, this would only reduce the slope calculation, thus providing a conservative estimate of this sensitivity in the water-limited part of the curve. When constructing the emergent constraint per pixel, only those ESMs that had relationships between *LST-Tair* and *SPEI* as well as g_c and *SPEI* with p-values < 0.1 were used to construct the constraint (Figures S5b and S5c in Supporting Information S1). Additionally, only timesteps of pixels that had an ESM LAI climatology of greater than or equal to 1 were used for each ESM, to ensure that the *LST* data reflected the temperature of a vegetated canopy rather than that of, for example, barren soil.

While the *SPEI* was used to represent moisture availability in this application, uncertainty in this index can be introduced due to the use of the Thornthwaite equation (Thornthwaite, 1948) to calculate potential evapotranspiration. Therefore to ensure the robustness of our methodology, we also performed the constraint using surface soil moisture anomalies, calculated from the Consistent Artificial-Intelligence based Soil Moisture (CASM) data set (Skulovich & Gentine, 2023) to represent moisture availability (Figure S8 in Supporting Information S1). The data was first converted to anomalies (the seasonal cycle was removed) before calculating the sensitivities, for consistency with *SPEI*, which is an index that reflects moisture anomalies. Using this data set provided similar results to using *SPEI* related to the ESM underestimation of γ^m_{gc} and its spatial distribution. The CASM data set was not used for the main analyses, as this data set reflects the moisture in only the top layer of the soil and not that of the entire root zone, which is more relevant for detecting plant water stress. For example, one region where the sensitivities are not as strong using the CASM data to calculate γ^m_{gc} was in Eastern Australia, and this is a region that has rooting depth in some locations of greater than 9 m (Stocker et al., 2021, 2023).

2.3. The Observational Constraint

To constrain the CMIP6 ESM estimates of γ^m_{gc}, we used a total of nine observational and reanalysis data sets to calculate the sensitivity of *LST-Tair* to *SPEI* ($\gamma^m_{LST-Tair}$) during the growing season (3 data sets for *LST*, 3 data sets for *Tair*, and 3 data sets for precipitation; Table S2 in Supporting Information S1). We chose to use multiple data sets for each variable to average out biases that might be present in a particular data source, and to allow for a quantification of uncertainty in the constraint (Figure S9 in Supporting Information S1). Similar to the ESM analysis, $\gamma^m_{LST-Tair}$ was based on a linear regression per pixel between *LST-Tair* anomalies and *SPEI*, and the growing season was defined as months where the monthly temperature climatology was greater than 278K (using *Tair* data from the 5th generation of the European Centre for Medium-Range Weather Forecasts atmospheric reanalysis of the global climate; ERA5, Hersbach et al., 2023) and the monthly net radiation climatology was at least 60% of its maximum monthly climatological value (calculated using data from Clouds and the Earth's Radiant Energy System; CERES).

For temperature data sets, *Tair* monthly data were used from ERA5, the Global Historical Climatology Network (GHCN) (Fan & Van Den Dool, 2008), and the Climate Research Unit (CRU) (Harris et al., 2020). For *LST*, monthly data were used from the Moderate Resolution Imaging Spectroradiometer (MODIS) 11 version 6.1 (retrieved using a split-window algorithm) (Wan, 2019), MODIS 21 version 6.1 (retrieved using an Advanced Spaceborne Thermal Emission and Reflection Radiometer Temperature/Emissivity Separation technique) (Hulley, 2021), and the Atmospheric Infrared Sounder (AIRS) version 7 (AIRS Project, 2019) that spanned 2003–2020. For MODIS 11, data from both the AQUA and TERRA satellites were averaged when all time steps were available on a given day (2 measurements from 2 satellites per day for a total of 4 daily measurements), while in the case of missing timesteps, only data from the satellite with both measurements available were used for that day's measurements. For MODIS 21, only data from the AQUA satellite was used since the TERRA satellite data had a detector for thermal band 29 fail in 2006 leading to striping in the final product (Hulley et al., 2019). Since the MODIS 21 level 3 product has not been filtered for dust (contrary to MODIS 11), daily measurements were removed from the monthly average calculation that had over a 2-degree Kelvin error associated with them which were labeled as having "poor performance".

Because *LST* data is derived from thermal infrared measurements, the observational *LST* data is only reflective of clear-sky conditions, while ESM *LST* data reflects all-sky conditions. To ensure that this was not biasing our

results, for four ESMs we calculated monthly *LST* data from daily data using all days, and then using only the 5 days with the maximum net radiation values (assumed to reflect clear-sky conditions). Using both formulations we then calculated $\gamma^m_{LST-Tair}$ and compared these to the median observational $\gamma^m_{LST-Tair}$ (Figure S10 in Supporting Information S1). While there was slightly more variability when calculating $\gamma^m_{LST-Tair}$ using only the maximum daily values, this was still much less than that of the observational data.

To represent moisture availability, we calculated the *SPEI* from monthly precipitation and *Tair* data using the R package "SPEI" (Beguería & Vicente-Serrano, 2023). For precipitation, we used data from the Global Precipitation Climatology Project (GPCP), the Global Precipitation Climatology Centre (GPCC), and CRU. For *Tair*, we used those same data sets listed above. We used 30 years of data which spanned 1990–2019 for *SPEI* calculated with GPCC, and 1991–2020 for *SPEI* calculated with GPCP and CRU due to the different data availability for each product. Similar to the ESM analysis, the Thornthwaite equation was used to calculate potential evapotranspiration, and the *SPEI* was calculated based on a log-logistic distribution function at a 12-month timescale.

To constrain γ^m_{gc} across the ESMs, the median $\gamma^m_{LST-Tair}$ across the observational data sets was used (Figure S3 in Supporting Information S1). To calculate the median $\gamma^m_{LST-Tair}$, only those observational data sets that had relationships between *LST-Tair* and *SPEI* with a p-values < 0.1 were used (Figure S5d in Supporting Information S1). Additionally, similar to the ESMs, only those timesteps of pixels that had an LAI climatology (Mao & Yan, 2019) greater than or equal to 1 were used, to ensure that the *LST* data reflected the temperature of a vegetated canopy. To depict the uncertainty in this constraint, the median plus and minus one standard deviation was also used to constrain γ^m_{gc} across the ESMs (Figure S9 in Supporting Information S1). All temperature and precipitation observational data sets used for calculating the constraint are displayed in Table S2 in Supporting Information S1.

The emergent constraint was applied pixel-by-pixel to provide a regional understanding (Figure S3 in Supporting Information S1). The R^2 values for each pixel are displayed in Figure S4 in Supporting Information S1.

2.4. Random Forest Algorithm and Shapley Values

To investigate whether there were certain climate characteristics that were common to regions where ESMs were underestimating these sensitivities, a random forest algorithm (RF) was applied using the R package "ranger" (Wright & Ziegler, 2017). The RF was designed to understand the ecosystem characteristics of regions where ESMs were underestimating γ^m_{gc}. Thus, first we calculated the difference between the median of the observationally constrained γ^m_{gc} and the median of the unconstrained γ^m_{gc} sensitivity in the CMIP6 ESMs (Figure 1c). Then to create our RF response variable, we converted these differences to categorical variables that were equal to negative 1 if these values were negative, 0 if the pixel was not significant at a p-value < 0.05, and positive 1 if the difference was positive (Figure S11 in Supporting Information S1).

For predictors we used variables related to both climate and ecosystem characteristics (Table S3 and Figure S12 in Supporting Information S1). Variables were removed that had correlations greater than 0.7 with other predictors (except for LAI which had a correlation over 0.7 with aridity index (AI), but was used to define the significant pixels), and recursive feature elimination was used to eliminate predictors that did not add any additional predictive power. The number of trees used (capped at a maximum of 1,000) and the number of variables to split at each node (between 2 and the total number of predictor variables) were optimized to produce the lowest out-of-bag error (based on approximately one third of the observations, Breiman, 2001). The prediction errors of the final RF are shown in Figure S11 in Supporting Information S1.

Shapley values were generated using the R-package "fastshap" (Greenwell, 2023) to understand how each predictor influenced the prediction of these regions. Shapley values decompose anomalies in the response variable of a model (the difference between an individual prediction and the mean model prediction) into components measuring the contributions of each predictor to the anomaly (Hart, 1989; Štrumbelj & Kononenko, 2014). In the case of a categorical response variable, each predictor's Shapley values reflect how that predictor is influencing the probability of a certain predicted outcome. For example, in the RF applied here, a Shapley value greater than 0 indicates that for that particular location, that predictor is increasing the probability that the unconstrained ESMs are underestimating γ^m_{gc} relative to the constrained value, while a value of less than 0 indicates that the predictor is decreasing the probability that the unconstrained ESMs are underestimating γ^m_{gc} relative to the constrained value.

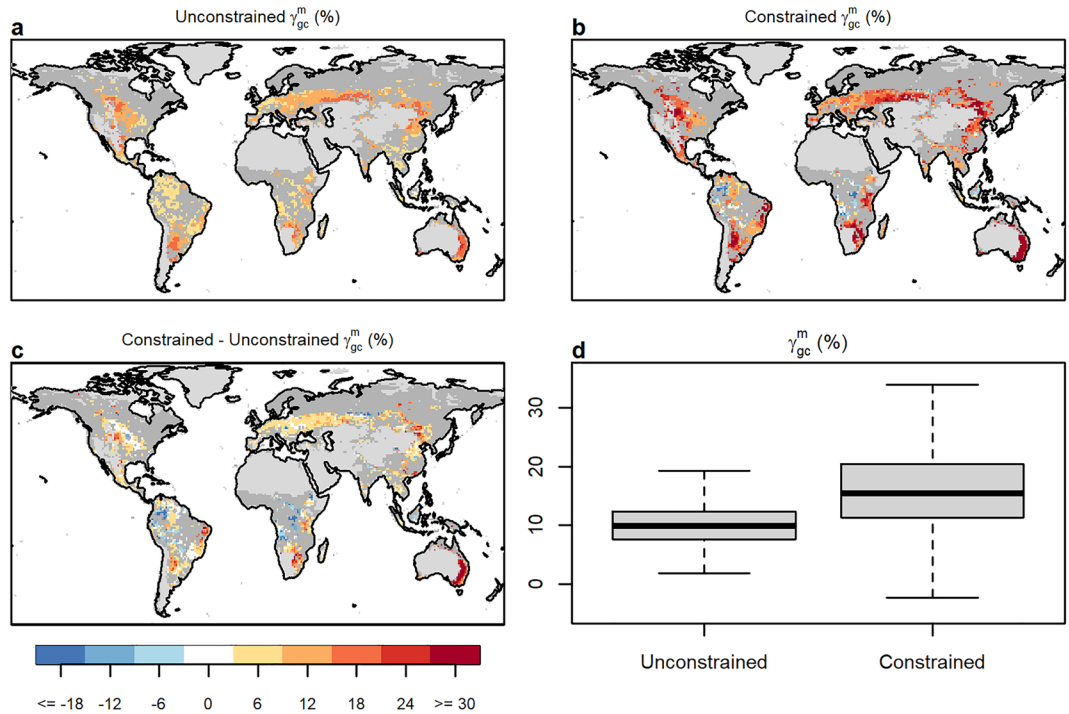

Figure 1. *Canopy conductance sensitivity to changes in moisture availability*. (a) The median unconstrained value of γ_{gc}^{m} across Coupled Model Intercomparison Project Phase 6 (CMIP6) Earth System Models (ESMs), (b) the median constrained value of γ_{gc}^{m} across CMIP6 ESMs, (c) the difference between subplots (a, b), and (d) a corresponding boxplot showing the distributions of subplots (a, b). In subplot (b), γ_{gc}^{m} in ESMs is constrained by the median value of 27 observational data set combinations. Light gray pixels are regions that were not analyzed due to the climatological leaf area index in observations never exceeding 1. Darker gray pixels are regions that were not analyzed because they did not have a significant relationship between γ_{gc}^{m} and $\gamma_{LST-Tair}^{m}$ across the ensemble of ESMs at a p-value < 0.05. Only growing season data were used, defined using the local monthly climatology of net radiation and *Tair* (see Materials and Methods). In the boxplots, the horizontal lines represent the first quartile, median, and third quartile of the map distributions. The bars extend to -1.5 and $+1.5$ times the interquartile range.

A Shapley value of 0 indicates that the predictor is not providing useful information to predict the categorical response variable.

2.5. Assessing Climate Feedbacks

To understand how the underestimation of γ_{gc}^{m} in ESMs was feeding back on projections of global climate, for each ESM we indexed time periods when the local *SPEI* was greater than 1 (anomalously wet periods) and when the *SPEI* was less than -1 (anomalously dry periods). We then used these indexed values to calculate an average ESM value of *GPP*, *Tair*, and transpiration during both these dry and wet periods across all regions where our emergent constraint had significant results and examined their difference in Figures 3a–3c. We repeated the analysis using an *SPEI* less than -2 for at least 3-month which resulted in similar trends though more variable (see Figures 3d–3f). Those ESMs that had *GPP* data available are listed in Table S1 in Supporting Information S1. We also compared LAI values between the dry and wet periods, by computing the difference between the average LAI during timesteps when *SPEI* was greater than 1, and the average LAI during timesteps when *SPEI* was less than -1, to determine if ESMs showed an LAI response to drought. We used a paired student *t*-test to determine whether there were statistical changes in LAI between these anomalously wet and dry periods in the ESMs.

3. Results and Discussion

3.1. Canopy Conductance Sensitivity to Moisture Availability in ESMs

The unconstrained ESMs showed a positive sensitivity (meaning lower water availability led to lower canopy conductance) across all regions where g_c and *SPEI* had a significant relationship (p-value < 0.05), and the data

could be constrained (Figure 1a). This is consistent with widely observed plant behavior, that most plants will reduce their stomatal openings during periods of low water availability, to reduce the risk of hydraulic failure (Konings & Gentine, 2017). γ^m_{gc} unconstrained had a median sensitivity of ~10% change per unit *SPEI* (expressed in figures and text as units of % since *SPEI* is unitless) in all regions where the emergent constraint showed significant results (p-value < 0.05), and maximum values in eastern Australia, a region known to have relatively higher isohydricity (stomatal regulation) than other regions of significance for the constraint, such as the U.S. cornbelt (Konings & Gentine, 2017) (Figures 1a and 1d).

The linear relationship we identified between γ^m_{gc} and $\gamma^m_{LST-Tair}$ across ESMs allowed us to use observationally derived estimates of $\gamma^m_{LST-Tair}$ to infer constrained estimates of γ^m_{gc} across approximately 17% of the vegetated regions of the globe (Figure 1b). The resulting constrained estimates of γ^m_{gc} had a median sensitivity of ~15% change in g_c per unit *SPEI*, demonstrating a consistent ESM underestimation of γ^m_{gc} (Figure 1). The strongest underestimation of γ^m_{gc} was in Eastern Australia (underestimated by ≥30% change in g_c per unit *SPEI*), while other regions of underestimation were the Central United States, Western and Central Europe, Southeastern Brazil, Argentina, Southern Africa, as well as in Northeastern China and Mongolia (Figure 1, and Figures S4 and S9 in Supporting Information S1). Our results show that γ^m_{gc} can be underestimated in the unconstrained ESMs by as much as 50%, with a median underestimation of sensitivity of ~33% compared to the constrained ESM values (i.e., a 10% change in g_c per unit *SPEI* vs. a 15% change in g_c per unit *SPEI*). The spatial variability of the observationally constrained γ^m_{gc} was also much greater than what the unconstrained data showed (an interquartile range of ~11% vs. ~5%), suggesting that ESMs are not capturing the complete range of ecosystem stomatal responses to moisture limitation (e.g., fully isohydric to fully anisohydric).

3.2. Characteristics of Constrained Regions

The emergent constraint we identified here is based on the relationship between γ^m_{gc} and $\gamma^m_{LST-Tair}$, but this relationship was only statistically significant for certain regions of the world (~17%). This is to be expected and is primarily due to the differential controls on ecosystem function across the water-energy limitation spectrum. For instance, predominantly energy-limited ecosystems would not be expected to exhibit a strong relationship between g_c, *SPEI* and *LST-Tair*. In an ecosystem where photosynthesis is limited by radiation, and where water supply tends to be non-limiting, there would be no response of g_c and *LST-Tair* to changes in water availability, and thus there would no longer be the physical and statistical relationships needed for an emergent constraint to be reliably applied in those regions. Similarly, ecosystems with a relatively high proportion of bare ground, and thus low vegetation control on the surface energy balance, would not be expected to exhibit a strong physical relationship between g_c and *LST-Tair*. Thus, while we performed this analysis globally, certain filters were used to ensure a robust emergent constraint which reduced the areas where the emergent constraint formulations could be applied. First, an LAI filter of 1 was used to mask out those pixels that had sparse vegetation, thus preventing the contamination of the *LST* signal from non-vegetated surfaces (Figure S5a in Supporting Information S1). Second, if an ESM did not have a relationship between g_c and *SPEI* or *LST-Tair* and *SPEI* with a p-value < 0.1, then that ESM was not used to compute the emergent constraint for that pixel (Figures S5b and S5c in Supporting Information S1). Third, if the relationship between γ^m_{gc} and $\gamma^m_{LST-Tair}$ was not significant across the ensemble of ESMs (p-value < 0.05) for a particular pixel then the result was excluded from the analysis. And fourth, only those observational data set combinations with relationships between *SPEI* and *LST-Tair* with p-values < 0.1 were used for each pixel constraint (Figure S5d in Supporting Information S1). Applying these filters was appropriate to ensure that the physical and statistical relationship necessary for an emergent constraint was present for each location where it was computed.

Thus, to better understand the characteristics of the regions where the emergent constraint could be applied, and where ESMs underestimated γ^m_{gc}, we used a random forest algorithm (RF) classification combined with Shapley values using environmental data as inputs to predict those regions (see Materials and Methods). Shapley values quantify the contribution of each predictor variable to each RF prediction (Hart, 1989). We used predictor variables that could be influential to γ^m_{gc}, including data sets related to climate (e.g., *Tair*), aboveground vegetation structure (e.g., maximum *LAI*), belowground vegetation structure (e.g., average rooting depth), and vegetation physiology (e.g., maximum carboxylation rate). The most important predictors in this analysis were the AI, *Tair*, and LAI (Figure 2). The RF and Shapley results showed that those regions of ESM underestimation were located primarily in dry sub-humid and semi-arid environments (AI between 0.2 and 0.65), and bordering regions that

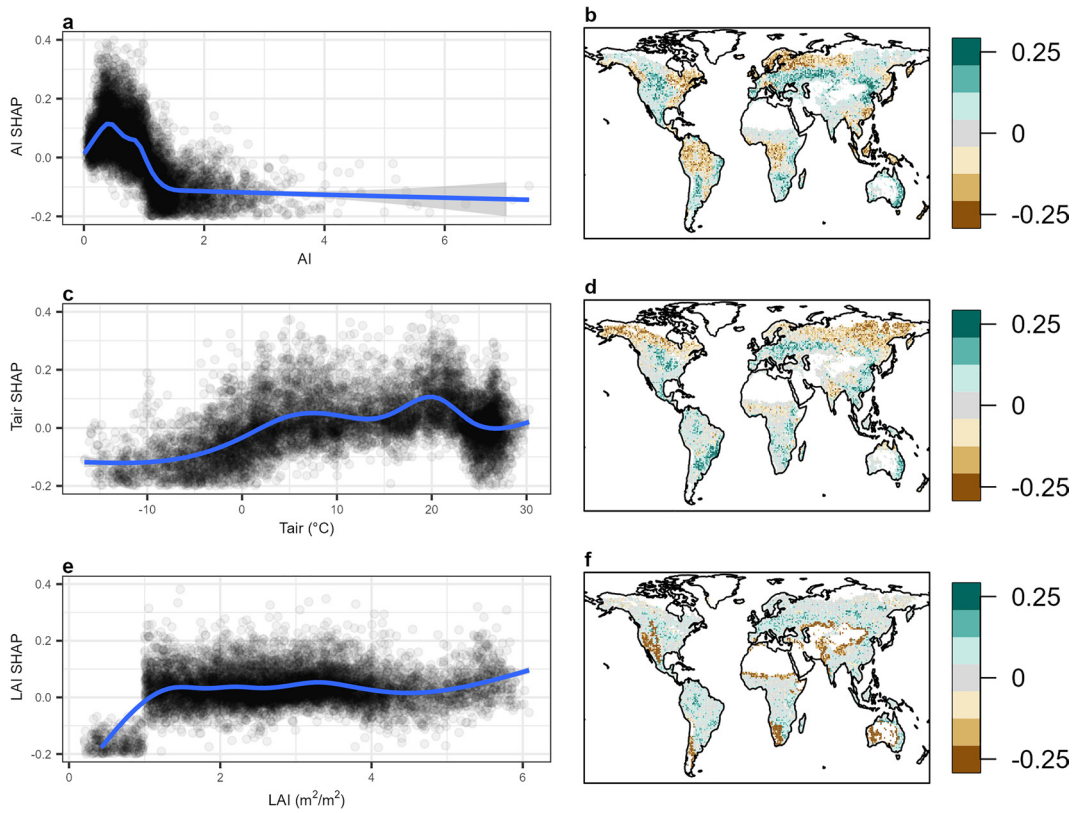

Figure 2. *Shapley values of the top three random forest predictors for the underestimation of* γ_{gc}^{m}. The Shapley (SHAP) values for the top three random forest predictors used to predict regions of Earth System Model (ESM) underestimation of γ_{gc}^{m}. These are the aridity index shown both as a scatter plot (a) and a corresponding map (b), the mean annual near-surface air temperature (*Tair*) as a scatter plot (c) and its corresponding map (d), and the maximum local leaf area index as a scatter plot (e), and its corresponding map (f). Positive SHAP values mean the examined factor has increasing probability to cause ESMs to underestimate γ_{gc}^{m}, while negative SHAP values mean the opposite. White regions of the maps in subplots (b, d, and f) are those regions that were missing data from at least one of the random forest predictor data sets.

transition to more humid environments, on average with an AI less than 1 (Figures 1 and 2 and Figures S11 and S12 in Supporting Information S1). These regions tend to be water-limited grasslands, croplands and savannas, with mean annual temperatures between 5 and 25 degrees Celsius, and with an LAI greater than 1. These findings show that ESMs are not reducing g_c enough during drought in regions of these characteristics, which is due to a lack of stomatal closure in response to soil dryness. In other words, in these regions, ESMs are depicting vegetation as more anisohydric than they truly are.

3.3. Implications for Carbon, Water, and Energy Fluxes

The general underestimation of γ_{gc}^{m} has implications for the exchange of carbon, water and energy fluxes in ESMs. In terms of the carbon cycle, we see that ESMs that most strongly underestimate the overall γ_{gc}^{m}, are also those ESMs that most severely underestimate the reduction in *GPP* during moderately dry events, defined by an $SPEI \leq -1$ (Figure 3a). This means that ESMs are likely overestimating *GPP* during these anomalously dry periods (reducing *GPP* by approximately 1 $gC/m^2/d$ rather than potentially double that). We also found that ESMs that most strongly underestimate the overall γ_{gc}^{m}, have a smaller increase in *Tair* during moderately dry events than what the constrained data implies (~1.25°C vs. 1.75°C) (Figure 3b), which is likely connected to an underestimation in the reduction of transpiration during dry events, which we also identified (~−0.1 vs. −0.35 $mmol.m^{-2}s^{-1}$) (Figure 3c). Although this might seem contrary to the well-established warm and dry bias of ESMs in the Central United States across multiple CMIP generations (Y. Lin et al., 2017; Mueller & Seneviratne, 2014), it has been demonstrated that these biases mainly stem from the misrepresentation of precipitation and resulting land-atmosphere interactions, rather than from the vegetation response to drought (Y. Lin

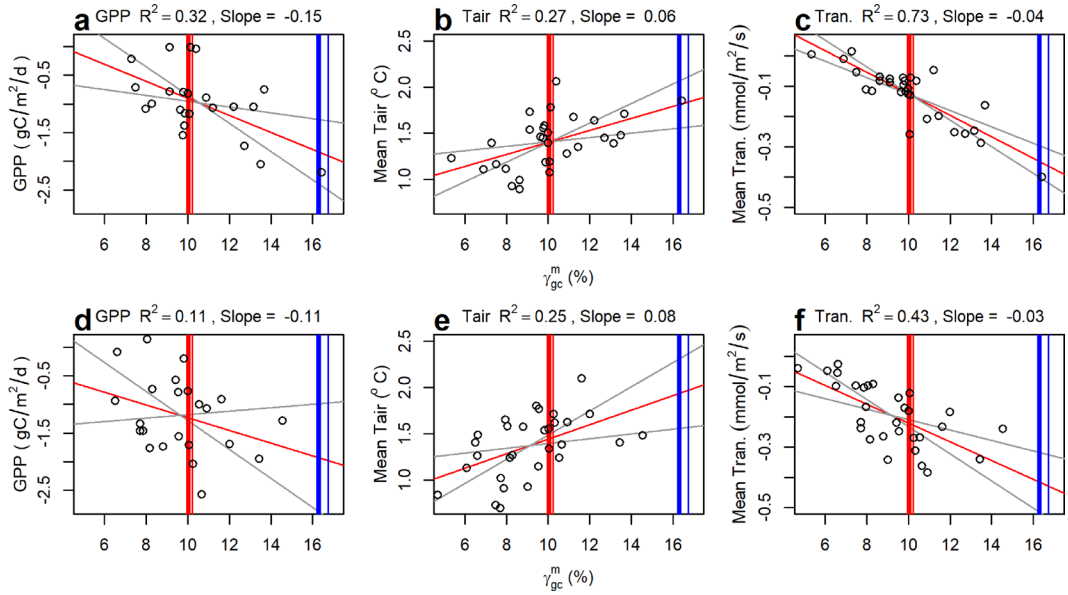

Figure 3. *Relationships between unconstrained Earth System Model (ESM) γ^m_{gc} and environmental variables averaged over dry periods*. The relationship between the mean unconstrained γ^m_{gc} per ESM and the difference between wet and moderately dry periods for *GPP* (a), *Tair* (b), and transpiration (c), as well as wet and extremely dry periods for *GPP* (d), *Tair* (e), and transpiration (f). Wet periods are defined as months when SPEI ≥ 1, while moderately dry periods are defined as months when SPEI ≤ -1, and extremely dry periods are defined by months when SPEI ≤ -2 for a minimum of 3-months. The linear relationships depicted in (a–c, e, and f) are significant at a p-value < 0.01. Each point represents the mean values for a particular ESM over the regions where ESMs are significantly (p-value < 0.05) underestimating γ^m_{gc} (see Figure 1). Data are confined to the growing season which is defined by the local monthly climatology of net radiation and *Tair* (see Materials and Methods). The diagonal red line in the scatter plots represents the best fit linear relationship based on ordinary least squares regression, while the gray diagonal lines represent the 95% confidence intervals. The thick red vertical line is the unconstrained ESM median and mean values for γ^m_{gc}, while the thick blue vertical line is the median and the thin blue line is the mean of γ^m_{gc} for the constrained ESMs (see Figure 1).

et al., 2017). Furthermore, our findings support reports showing the overestimation of *LE* by ESMs, that has been demonstrated consistently across biome types in CMIP6, and has been associated with biases in LAI, a main driver of γ^m_{gc} (Yuan et al., 2022). Here we show that this overestimation occurs in particular during these moderately dry episodes.

When we extend this analysis to only focus on extremely dry time periods (*SPEI* ≤ -2 for a minimum of 3 months), we see that the strength of the relationship between γ^m_{gc} and these climactic variables weakens (Figures 3d–3f). The results for *GPP* are no longer statistically significant at a p-value < 0.05, and the relationships between γ^m_{gc} and *Tair*, as well as γ^m_{gc} and transpiration have lower R^2 values than for during moderately dry periods. This indicates that an ESM underestimation of γ^m_{gc} during extreme droughts leads to more variable responses across the ESMs. On one hand, an underestimation of γ^m_{gc} during a prolonged extreme drought could lead to the depletion of soil moisture supplies resulting in a greater risk of hydraulic failure for vegetation, potentially resulting in reduced *GPP*, lower transpiration rates, and higher temperatures. However, only several of the ESMs incorporate processes related to plant hydraulics (e.g., CESM2 and NorESM2 ESMs which incorporate CLM5 as their land surface model) (Kennedy et al., 2019). On the other hand, if soil moisture supplies do not become limiting and hydraulic conductance remains unaffected, then this would result in vegetation with lower γ^m_{gc} continuing to have greater *GPP*, greater transpiration rates, and lower temperatures than those ESMs with greater γ^m_{gc} which has also been observed (Roman et al., 2015). In conclusion, this mixed response across ESMs is likely due to the variation in complexity of each ESM's land surface component (the resistance of different vegetation plant functional types to xylem embolism and whether i.e., represented), and how they represent the depletion of soil moisture. Additionally, less regions and time periods meet the extreme drought criteria (*SPEI* ≤ -2 for 3-month) across the ESMs, leading to a smaller sample size per ESM to average over, and a smaller range of values for γ^m_{gc}, which also likely contributes to lower R^2-values and higher p-values.

The misrepresentation of γ_{gc}^{m} across ESMs also leads to inaccurate biosphere-atmosphere feedbacks, reducing the ability of ESMs to represent extreme events accurately. Biosphere-atmosphere interactions contribute to the persistence of droughts and heatwaves (Yin et al., 2014), because transpiration can be a moisture source for future rainfall events. In fact, it has been shown that in water-limited ecosystems sustained transpiration assists in supplying water for precipitation during dry periods (Miralles et al., 2016). Therefore, on one hand, if transpiration is not reduced in ESMs as strongly as it should be during a moderate drought, the projected droughts and heatwaves may be shorter than would be expected in regions of strong biosphere-atmosphere feedbacks, due to the unrealistically sustained moisture source available for future rainfall events. On the other hand, if transpiration is unrealistically sustained in ESMs during a strong drought, the projected droughts and heatwaves may be prolonged due to the impact of sustained transpiration on reducing surface soil moisture, ultimately leading to a reduction in latent heat flux. Thus, ESMs may not fully capture the extent of droughts and heatwaves due to this misrepresentation of the response of canopy conductance to moisture availability.

4. Conclusions

There are various reasons for why ESMs might underestimate both the local γ_{gc}^{m} as well as its spatial variability. First, it is well documented that LAI in ESMs is highly variable with ESM-to-ESM biases (Collier et al., 2018) and does not agree well with observation-based data sets, leading to higher or lower g_c accordingly (e.g., an overestimation of LAI would likely lead to an overestimation of g_c). Second, it has been shown that certain ESMs over-estimate the impact of LAI on vegetation conductance leading to the underestimation of the mean value of g_c (Zhang et al., 2022). Meanwhile, ∼30% of the ESMs show no significant change in LAI during drought events compared to wetter than average periods using a paired sample *t*-test (p-value < 0.05), although loss of leaves and wilting are commonly observed for particular plant functional types in response to drought (Munné-Bosch & Alegre, 2004). This reduction in LAI observed in nature would lead to reduced g_c during drought simply due to less leaves being present, and the absence of this response in ESMs would likely lead to g_c being overestimated during drought. Third, the majority of ESMs do not account for xylem transport limitations or hydraulic transport processes (Y.-S. Lin et al., 2015), and these traits directly impact anisohydricity (Sperry & Love, 2015). Fourth, transpiration is underestimated for most ESMs, which translates to the effects of vegetation regulation on the surface energy balance being underestimated (Lian et al., 2018). Fifth, stomatal conductance is often represented empirically or semi-empirically in ESMs based on leaf level equations (e.g., the Ball-Berry-Leuning model, Ball et al., 1987; Dewar, 2002), with set parameterizations that are not able to account for the various water stress coping mechanisms that different types of vegetation employ. And while representations based on stomatal optimization principles (the idea that plants optimize their carbon gain per a set amount of water lost) were developed several decades ago (Farquhar & Cowan, 1977), difficulties arose when defining the optimization criteria (Sperry et al., 2017). More recently, it has become increasingly commonplace to incorporate improved optimization based g_c implementations in ESMs (e.g., the Medlyn model, Medlyn et al., 2011), but these approaches typically do not include mechanistic descriptions of soil moisture dependencies, and instead rely on poorly constrained empirical modifiers (Franks et al., 2017). While this variability between ESMs contributes to the overall ESM spread, these differences allow for the use of an emergent constraint for this application (Williamson et al., 2021).

It should also be noted that changes in factors other than g_c, in response to water availability changes, could influence the results presented here. In particular, changes in aerodynamic conductance (g_a) in response to water availability changes could affect the derived relationship between γ_{gc}^{m} and $\gamma_{LST-Tair}^{m}$. The formulation we used to calculate g_c for this analysis is based on Fick's law (see Materials and Methods), and thus includes the effects of g_a in its calculation. However, changes in g_c during drought periods are dominated by the effects of stomatal closure in ESMs (Figures S6 and S7 in Supporting Information S1). This was verified using an inversion of the Penman-Monteith equation (Monteith, 1965; Penman, 1948) (see Materials and Methods), which allowed us to separately calculate g_c and g_a and then determine their sensitivities to moisture availability. The γ_{gc}^{m} calculated via the Penman-Monteith equation showed a strong relationship between it and γ_{gc}^{m} calculated via Fick's Law (an average RMSE across four ESMs of 3.78), and a much weaker relationship between γ_{ga}^{m} calculated via the Penman-Monteith equation and γ_{gc}^{m} calculated by Fick's Law (an average RMSE across four ESMs of 13.36).

Another potential cause of discrepancy between modeled and constrained γ_{gc}^{m} could stem from differences between ESM and observational *LST* measurements. Observational *LST* data is reflective of clear-sky conditions, while ESM *LST* data is reflective of all-sky conditions. However, we confirmed that this difference in *LST*

measurements is largely not responsible for the underestimation of γ_{gc}^{m} (see Materials and Methods; Figure S10 in Supporting Information S1).

It should be noted that the constrained γ_{gc}^{m} presented here is also likely a conservative low-end estimate. The relationship between g_c and water availability varies, and there tends to be a faster rate of change in g_c when water supply or demand becomes limiting (Feldman et al., 2018; Green et al., 2019). Therefore, by using a linear simplification of γ_{gc}^{m}, the most extreme canopy conductance responses are likely underestimated.

In conclusion, our results provide the first observationally based estimate of global canopy conductance sensitivity to changes in moisture availability, establishing a new benchmark standard for CMIP6 ESMs. By developing a novel emergent constraint, we avoid the need for regional and global g_c observations to evaluate ESM performance for γ_{gc}^{m}. Our results underscore that CMIP6 ESMs underestimate γ_{gc}^{m} due to incorrect relative changes in g_c that occur in response to drought. Our results emphasize the need to improve plant hydraulics, plant traits, and vegetation dynamics in ESMs for more precise projections of stomatal behavior and to improve the g_c response to drought (Anderegg & Venturas, 2020; Harper et al., 2021; Kennedy et al., 2019). Because g_c regulates carbon, water and energy fluxes, improving the representation of γ_{gc}^{m} in ESMs should advance their ability to represent climate extremes and carbon uptake accurately, which is increasingly important as both the intensity and frequency of climate extremes are expected to change in the coming decades.

Conflict of Interest

The authors declare no conflicts of interest relevant to this study.

Data Availability Statement

The remote sensing, reanalysis, and ESM data used in this study are freely available from the following locations:

- AIRS land surface temperature (AIRS Project, 2019): https://disc.gsfc.nasa.gov/datasets/AIRS3STM_7.0/summary?keywords=airs%20version%207
- CERES net radiation (Wielicki et al., 1996): https://ceres-tool.larc.nasa.gov/ord-tool/jsp/EBAF42Selection.jsp
- CMIP6 historical simulations: https://esgf-node.llnl.gov/search/cmip6/
- CRU precipitation, near surface air temperature, and potential evaporation (Harris et al., 2020): https://catalogue.ceda.ac.uk/uuid/c26a65020a5e4b80b20018f148556681
- ERA5 near surface air temperature (Hersbach et al., 2023): https://cds.climate.copernicus.eu/cdsapp#!/dataset/reanalysis-era5-single-levels-monthly-means?tab=overview
- ETOPO5 elevation (Sloss, 1995): https://iridl.ldeo.columbia.edu/SOURCES/.NOAA/.NGDC/.ETOPO5/datasetdatafiles.html?Set-Language=en
- GHCN CAMS near surface air temperature (Fan & Van Den Dool, 2008): https://psl.noaa.gov/data/gridded/data.ghcncams.html
- Global mean leaf area index climatology, 1981–2015 (Mao & Yan, 2019): https://daac.ornl.gov/cgi-bin/dsviewer.pl?ds_id=1653 JULY 8 2022
- GPCC precipitation (Schneider et al., 2011): https://opendata.dwd.de/climate_environment/GPCC/full_data_monthly_v2020/25/
- GPCP precipitation (Pendergrass & NCAR, 2016): https://www.ncei.noaa.gov/data/global-precipitation-climatology-project-gpcp-monthly/access/
- MODIS 11 land surface temperature (Wan, 2019): https://lpdaac.usgs.gov/products/mod11c3v061/
- MODIS 21 land surface temperature (Hulley, 2021): https://lpdaac.usgs.gov/products/myd21v061/
- MODIS land cover type (Friedl & Sulla-Menashe, 2018): https://lpdaac.usgs.gov/products/mcd12c1v006/
- Rooting depth (Stocker et al., 2021, 2023): https://doi.org/10.5281/zenodo.5515246
- Temperature Standardized maximum carboxylation rate (Luo et al., 2021): https://zenodo.org/record/5090497#.Y3fX4cfMKF4
- WorldClim bioclimatic variables (Fick & Hijmans, 2017): https://www.worldclim.org/data/worldclim21.html

"CMIP6 model data produced by the Modeling Centers listed in Table S1 in Supporting Information S1 is licensed under a Creative Commons Attribution-ShareAlike 4.0 International License (https://creativecommons.org/licenses/). Consult https://pcmdi.llnl.gov/CMIP6/TermsOfUse for terms of use governing CMIP6 output,

including citation requirements and proper acknowledgment. Further information about this data, including some limitations, can be found via the further_info_url (recorded as a global attribute in this file). The data producers and data providers make no warranty, either express or implied, including, but not limited to, warranties of merchantability and fitness for a particular purpose. All liabilities arising from the supply of the information (including any liability arising in negligence) are excluded to the fullest extent permitted by law."

The code and processed data to generate the main paper figures are provided here:
https://doi.org/10.6084/m9.figshare.23849073 (Green, 2023a)
https://doi.org/10.6084/m9.figshare.23849076 (Green, 2023b)
https://doi.org/10.6084/m9.figshare.23849079 (Green, 2023c)
https://doi.org/10.6084/m9.figshare.23849064.v2 (Green, 2023d)

Acknowledgments
JKG and TFK were supported by the Land Ecosystem Models based On New Theory, obseRvations and Experi-mEnts (LEMONTREE) project, funded through the generosity of Eric and Wendy Schmidt by recommendation of the Schmidt Futures programme. TFK acknowledges additional support from the RUBISCO Science Focus Area, which is sponsored by the Regional and Global Model Analysis (RGMA) Program in the Climate and Environmental Sciences Division (CESD) of the Office of Biological and Environmental Research (BER) in the U.S. Department of Energy (DOE) Office of Science, a DOE Early Career Research Program Award DE-SC0021023, and NASA Awards 80NSSC21K1705 and 80NSSC20K1801. Finally, JKG thanks Philippe Ciais for providing constructive feedback for the manuscript. All of the data analysis and figure generation for this study were performed in R (R Core Team, 2022) and R studio (Posit Team, 2023).

References

AIRS Project. (2019). Aqua/AIRS L3 monthly standard physical retrieval (AIRS-only) 1 degree x 1 degree V7.0 [Dataset]. Goddard Earth Sciences Data and Information Services Center (GES DISC). https://doi.org/10.5067/UBENJB9D3T2H

Anderegg, W. R. L., & Venturas, M. D. (2020). Plant hydraulics play a critical role in Earth system fluxes. *New Phytologist*, *226*(6), 1535–1538. https://doi.org/10.1111/nph.16548

Baldocchi, D. D., Luxmoore, R. J., & Hatfield, J. L. (1991). Discerning the forest from the trees: An essay on scaling canopy stomatal conductance. *Agricultural and Forest Meteorology*, *54*(2–4), 197–226. https://doi.org/10.1016/0168-1923(91)90006-C

Ball, J. T., Woodrow, I. E., & Berry, J. A. (1987). A model predicting stomatal conductance and its contribution to the control of photosynthesis under different environmental conditions. In J. Biggins (Ed.), *Progress in photosynthesis Research*. Springer.

Beguería, S., & Vicente-Serrano, S. M. (2023). SPEI: Calculation of the Standardized Precipitation-Evapotranspiration Index. R package version 1.8.1. Retrieved from https://CRAN.R-project.org/package=SPEI

Berry, J. A., Beerling, D. J., & Franks, P. J. (2010). Stomata: Key players in the earth system, past and present. *Current Opinion in Plant Biology*, *13*(3), 232–239. https://doi.org/10.1016/j.pbi.2010.04.013

Bonan, G. B., Patton, E. G., Finnigan, J. J., Baldocchi, D. D., & Harman, I. N. (2021). Moving beyond the incorrect but useful paradigm: Reevaluating big-leaf and multilayer plant canopies to model biosphere-atmosphere fluxes – A review. *Agricultural and Forest Meteorology*, *306*, 108435. https://doi.org/10.1016/j.agrformet.2021.108435

Bonan, G. B., Williams, M., Fisher, R. A., & Oleson, K. W. (2014). Modeling stomatal conductance in the earth system: Linking leaf water-use efficiency and water transport along the soil-plant-atmosphere continuum. *Geoscientific Model Development*, *7*(5), 2193–2222. https://doi.org/10.5194/gmd-7-2193-2014

Breiman, L. (2001). Random forests. *Machine Learning*, *45*(1), 5–32. https://doi.org/10.1201/9780367816377-11

Buckley, T. N. (2019). How do stomata respond to water status? *New Phytologist*, *224*(1), 21–36. https://doi.org/10.1111/nph.15899

Campbell, G., & Norman, J. (1998). *An introduction to environmental biophysics*. Springer-Verlag.

Collier, N., Hoffman, F. M., Lawrence, D. M., Keppel-Aleks, G., Koven, C. D., Riley, W. J., et al. (2018). The international land model benchmarking (ILAMB) system: Design, theory, and implementation. *Journal of Advances in Modeling Earth Systems*, *10*(11), 2731–2754. https://doi.org/10.1029/2018MS001354

Cox, P. M., Huntingford, C., & Williamson, M. S. (2018). Emergent constraint on equilibrium climate sensitivity from global temperature variability. *Nature*, *553*(7688), 319–322. https://doi.org/10.1038/nature25450

Dewar, R. C. (2002). The Ball-Berry-Leuning and Tardieu-Davies stomatal models: Synthesis and extension within a spatially aggregated picture of guard cell function. *Plant, Cell and Environment*, *25*(11), 1383–1398. https://doi.org/10.1046/j.1365-3040.2002.00909.x

Fan, Y., & Van Den Dool, H. (2008). A global monthly land surface air temperature analysis for 1948–present. *Journal of Geophysical Research*, *113*(D1), 2007JD008470. https://doi.org/10.1029/2007JD008470

Farella, M. M., Fisher, J. B., Jiao, W., Key, K. B., & Barnes, M. L. (2022). Thermal remote sensing for plant ecology from leaf to globe. *Journal of Ecology*, *110*(9), 1–19. https://doi.org/10.1111/1365-2745.13957

Farquhar, G. D., & Cowan, I. R. (1977). Stomatal function in relation to leaf metabolism and environment. In D. H. Jennings (Ed.), *Integration of activity in the higher plant* (pp. 471–505). Cambridge University Press.

Feldman, A. F., Short Gianotti, D. J., Konings, A. G., McColl, K. A., Akbar, R., Salvucci, G. D., & Entekhabi, D. (2018). Moisture pulse-reserve in the soil-plant continuum observed across biomes. *Nature Plants*, *4*(12), 1026–1033. https://doi.org/10.1038/s41477-018-0304-9

Fick, S. E., & Hijmans, R. J. (2017). WorldClim 2: New 1km spatial resolution climate surfaces for global land area. *International Journal of Climatology*, *37*(12), 4302–4315. https://doi.org/10.1002/joc.5086

Forzieri, G., Miralles, D. G., Ciais, P., Alkama, R., Ryu, Y., Duveiller, G., et al. (2020). Increased control of vegetation on global terrestrial energy fluxes. *Nature Climate Change*, *10*(4), 1–7. https://doi.org/10.1038/s41558-020-0717-0

Franks, P. J., Berry, J. A., Lombardozzi, D. L., & Bonan, G. B. (2017). Stomatal function across temporal and spatial scales: Deep-time trends, land-atmosphere coupling and global models. *Plant Physiology*, *174*(2), 583–602. https://doi.org/10.1104/pp.17.00287

Franks, P. J., Bonan, G. B., Berry, J. A., Lombardozzi, D. L., Holbrook, N. M., Herold, N., & Oleson, K. W. (2018). Comparing optimal and empirical stomatal conductance models for application in Earth system models. *Global Change Biology*, *24*(12), 5708–5723. https://doi.org/10.1111/gcb.14445

Friedl, M. A., & Sulla-Menashe, D. (2018). User guide to collection 6 MODIS land cover (MCD12Q1 and MCD12C1) product (Vol. 1–18).

Friedlingstein, P., Jones, M. W., O'Sullivan, M., Andrew, R. M., Bakker, D. C. E., Hauck, J., et al. (2022). Global carbon budget 2021. *Earth System Science Data*, *14*(4), 1917–2005. https://doi.org/10.5194/essd-14-1917-2022

Fu, Z., Ciais, P., Feldman, A. F., Gentine, P., Makowski, D., Prentice, I. C., et al. (2022). Critical soil moisture thresholds of plant water stress in terrestrial ecosystems. *Science Advances*, *8*(44), eabq7827. https://doi.org/10.1126/sciadv.abq7827

Green, J. K. (2023a). Code_to_generate_Figure1_to_Figure3 [Dataset]. figshare. https://doi.org/10.6084/m9.figshare.23849073

Green, J. K. (2023b). Processed_data_for_Figure1 [Dataset]. figshare. https://doi.org/10.6084/m9.figshare.23849076

Green, J. K. (2023c). Processed_data_for_Figure2 [Dataset]. figshare. https://doi.org/10.6084/m9.figshare.23849079

Green, J. K. (2023d). Processed_data_for_Figure3 [Dataset]. figshare. https://doi.org/10.6084/m9.figshare.23849064.v2

Green, J. K., Ballantyne, A., Abramoff, R., Gentine, P., Makowski, D., & Ciais, P. (2022). Surface temperatures reveal the patterns of vegetation water stress and their environmental drivers across the tropical Americas. *Global Change Biology*, *28*(9), 1–16. https://doi.org/10.1111/gcb.16139

Green, J. K., Konings, A. G., Alemohammad, S. H., Berry, J., Entekhabi, D., Kolassa, J., et al. (2017). Regionally strong feedbacks between the atmosphere and terrestrial biosphere. *Nature Geoscience*, *10*(May), 410–414. https://doi.org/10.1038/ngeo2957

Green, J. K., Seneviratne, S. I., Berg, A. M., Findell, K. L., Hagemann, S., Lawrence, D. M., & Gentine, P. (2019). Large influence of soil moisture on long-term terrestrial carbon uptake. *Nature*, *565*(7740), 476–479. https://doi.org/10.1038/s41586-018-0848-x

Greenwell, B. (2023). fastshap: Fast Approximate Shapley Values. R package version 0.1.0. Retrieved from https://CRAN.R-project.org/package=fastshap

Hall, A., Cox, P., Huntingford, C., & Klein, S. (2019). Progressing emergent constraints on future climate change. *Nature Climate Change*, *9*(4), 269–278. https://doi.org/10.1038/s41558-019-0436-6

Hall, A., & Qu, X. (2006). Using the current seasonal cycle to constrain snow albedo feedback in future climate change. *Geophysical Research Letters*, *33*(3), 1–4. https://doi.org/10.1029/2005GL025127

Harper, A. B., Williams, K. E., McGuire, P. C., Duran Rojas, M. C., Hemming, D., Verhoef, A., et al. (2021). Improvement of modeling plant responses to low soil moisture in JULESvn4.9 and evaluation against flux tower measurements. *Geoscientific Model Development*, *14*(6), 3269–3294. https://doi.org/10.5194/gmd-14-3269-2021

Harris, I., Osborn, T. J., Jones, P., & Lister, D. (2020). Version 4 of the CRU TS monthly high-resolution gridded multivariate climate dataset. *Scientific Data*, *7*(1), 1–18. https://doi.org/10.1038/s41597-020-0453-3

Hart, S. (1989). Shapley value. In J. Eatwell, M. Milgate, & P. Newman (Eds.), *Game theory* (pp. 210–216). Palgrave Macmillan. https://doi.org/10.1007/978-1-349-20181-5_25

Hersbach, H., Bell, B., Berrisford, P., Biavati, G., Horanyi, A., Munoz Sabater, J., et al. (2023). ERA5 monthly averaged data on single levels from 1940 to present [Dataset]. Copernicus Climate Change Service (C3S) Climate Data Store (CDS). https://doi.org/10.24381/cds.f17050d7

Hulley, G. (2021). MODIS/Aqua land surface temperature/3-band emissivity 5-min L2 1km V061 [Dataset]. NASA EOSDIS Land Processes DAAC. https://doi.org/10.5067/MODIS/MYD21.061

Hulley, G., Freepartner, R., Malakar, N., & Sarkar, S. (2019). Moderate resolution imaging spectroradiometer (MODIS) land surface temperature and emissivity product (MxD21) user guide (p. 37).

Humphrey, V., Berg, A., Ciais, P., Gentine, P., Jung, M., Reichstein, M., et al. (2021). Soil moisture–atmosphere feedback dominates land carbon uptake variability. *Nature*, *592*(7852), 65–69. https://doi.org/10.1038/s41586-021-03325-5

Jarvis, P. G., & Mcnaughton, K. G. (1986). Stomatal control of transpiration: Scaling up from leaf to region. *Advances in Ecological Research*, *15*(C), 1–49. https://doi.org/10.1016/S0065-2504(08)60119-1

Kennedy, D., Swenson, S., Oleson, K. W., Lawrence, D. M., Fisher, R., Lola Da Costa, A. C., & Gentine, P. (2019). Implementing plant hydraulics in the community land model, version 5. *Journal of Advances in Modeling Earth Systems*, *11*(2), 485–513. https://doi.org/10.1029/2018MS001500

Konings, A. G., & Gentine, P. (2017). Global variations in ecosystem-scale isohydricity. *Global Change Biology*, *23*(2), 891–905. https://doi.org/10.1111/gcb.13389

Leuning, R. (1995). A critical appraisal of a combined stomatal-photosynthesis model for C3 plants. *Plant, Celt and Environment*, *18*(4), 339–355. https://doi.org/10.1111/j.1365-3040.1995.tb00370.x

Lian, X., Piao, S., Huntingford, C., Li, Y., Zeng, Z., Wang, X., et al. (2018). Partitioning global land evapotranspiration using CMIP5 models constrained by observations. *Nature Climate Change*, *8*(7), 640–646. https://doi.org/10.1038/s41558-018-0207-9

Lin, Y., Dong, W., Zhang, M., Xie, Y., Xue, W., Huang, J., & Luo, Y. (2017). Causes of model dry and warm bias over central U.S. and impact on climate projections. *Nature Communications*, *8*(1), 1–8. https://doi.org/10.1038/s41467-017-01040-2

Lin, Y.-S., Medlyn, B. E., Duursma, R. A., Prentice, I. C., Wang, H., Baig, S., et al. (2015). Optimal stomatal behaviour around the world. *Nature Climate Change*, *5*(May), 1–6. https://doi.org/10.1038/nclimate2550

Luo, X., Keenan, T. F., Chen, J. M., Croft, H., Colin Prentice, I., Smith, N. G., et al. (2021). Global variation in the fraction of leaf nitrogen allocated to photosynthesis. *Nature Communications*, *12*(1), 1–10. https://doi.org/10.1038/s41467-021-25163-9

Mao, J., & Yan, B. (2019). *Global monthly mean leaf area index climatology, 1981-2015*. ORNL DAAC. https://doi.org/10.3334/ORNLDAAC/1653

Medlyn, B. E., Duursma, R. A., Eamus, D., Ellsworth, D. S., Prentice, I. C., Barton, C. V. M., et al. (2011). Reconciling the optimal and empirical approaches to modelling stomatal conductance: Reconciling optimal and empirical stomatal models. *Global Change Biology*, *17*(6), 2134–2144. https://doi.org/10.1111/j.1365-2486.2010.02375.x

Miralles, D. G., Nieto, R., McDowell, N. G., Dorigo, W. A., Verhoest, N. E., Liu, Y. Y., et al. (2016). Contribution of water-limited ecoregions to their own supply of rainfall. *Environmental Research Letters*, *11*(12), 124007. https://doi.org/10.1088/1748-9326/11/12/124007

Monteith, J. L. (1965). Evaporation and environment. In *Symposia of the society for experimental biology* (Vol. 19, pp. 205–234).

Mueller, B., & Seneviratne, S. I. (2014). Systematic land climate and evapotranspiration biases in CMIP5 simulations. *Geophysical Research Letters*, *41*(1), 128–134. https://doi.org/10.1002/2013GL058055

Munné-Bosch, S., & Alegre, L. (2004). Die and let live: Leaf senescence contributes to plant survival under drought stress. *Functional Plant Biology*, *31*(3), 203–216. https://doi.org/10.1071/FP03236

NCAR. (2016). In A. Pendergrass (Ed.), *The climate data guide: GPCP (monthly): Global precipitation climatology project*. Retrieved from https://climatedataguide.ucar.edu/climate-data/gpcp-monthly-global-precipitation-climatology-project

Penman, H. L. (1948). Natural evaporation from open water, bare soil and grass. *Proceedings of the Royal Society of London. Series A, Mathematical and Physical Sciences*, *193*, 120–145.

Posit Team. (2023). RStudio: Integrated development environment for R. Posit Software, PBC. Retrieved from http://www.posit.co/

R Core Team. (2022). R: A language and environment for statistical computing. R Foundation for Statistical Computing. Retrieved from https://www.R-project.org/

Roman, D. T., Novick, K. A., Brzostek, E. R., Dragoni, D., Rahman, F., & Phillips, R. P. (2015). The role of isohydric and anisohydric species in determining ecosystem-scale response to severe drought. *Oecologia*, *179*(3), 641–654. https://doi.org/10.1007/s00442-015-3380-9

Sabot, M. E. B., De Kauwe, M. G., Pitman, A. J., Medlyn, B. E., Ellsworth, D. S., Martin-StPaul, N. K., et al. (2022). One stomatal model to rule them all? Toward improved representation of carbon and water exchange in global models. *Journal of Advances in Modeling Earth Systems*, *14*(4), e2021MS002761. https://doi.org/10.1029/2021MS002761

Schneider, U., Becker, A., Finger, P., Meyer-Christoffer, A., Rudolf, B., & Ziese, M. (2011). GPCC full data reanalysis version 6.0 at 0.5°: Monthly land-surface precipitation from rain-gauges built on GTS-based and historic data [Dataset]. Stl. https://doi.org/10.5676/DWD_GPCC/FD_M_V7_050

Shiogama, H., Watanabe, M., Kim, H., & Hirota, N. (2022). Emergent constraints on future precipitation changes (Vol. 602). https://doi.org/10.1038/s41586-021-04310-8

Skulovich, O., & Gentine, P. (2023). A long-term consistent artificial intelligence and remote sensing-based soil moisture dataset. *Scientific Data*, *10*(1), 154. https://doi.org/10.1038/s41597-023-02053-x

Sloss, P. W. (1995). NOAA/NGDC data announcement 88-MGG-02. Bathymtery/topography data [Dataset]. NOAA/NESDIS/NGDC National Geophysical Data Center, NOAA. Retrieved from https://iridl.ldeo.columbia.edu/SOURCES/.NOAA/.NGDC/.ETOPO5/datasetdatafiles.html?Set-Language=en

Sperry, J. S., & Love, D. M. (2015). What plant hydraulics can tell us about responses to climate-change droughts. *New Phytologist*, *207*(1), 14–27. https://doi.org/10.1111/nph.13354

Sperry, J. S., Venturas, M. D., Anderegg, W. R. L., Mencuccini, M., Mackay, D. S., Wang, Y., & Love, D. M. (2017). Predicting stomatal responses to the environment from the optimization of photosynthetic gain and hydraulic cost. *Plant, Cell and Environment*, *40*(6), 816–830. https://doi.org/10.1111/pce.12852

Stocker, B. D., Tumber-Dávila, S. J., Konings, A. G., Anderson, M. B., Hain, C., & Jackson, R. B. (2021). Global rooting zone water storage capacity and rooting depth estimates (v1.0) [Dataset]. Zenodo. https://doi.org/10.1101/2021.09.17.460332

Stocker, B. D., Tumber-Dávila, S. J., Konings, A. G., Anderson, M. C., Hain, C., & Jackson, R. B. (2023). Global patterns of water storage in the rooting zones of vegetation. *Nature Geoscience*, *16*(3), 250–256. https://doi.org/10.1038/s41561-023-01125-2

Štrumbelj, E., & Kononenko, I. (2014). Explaining prediction models and individual predictions with feature contributions. *Knowledge and Information Systems*, *41*(3), 647–665. https://doi.org/10.1007/s10115-013-0679-x

Thornthwaite, C. W. (1948). An approach toward a rational classification of climate. *Geographical Review*, *38*(1), 55–94. https://doi.org/10.2307/210739

Trugman, A. T., Medvigy, D., Mankin, J. S., & Anderegg, W. R. L. (2018). Soil moisture stress as a major driver of carbon cycle uncertainty. *Geophysical Research Letters*, *45*(13), 6495–6503. https://doi.org/10.1029/2018GL078131

Vicente-serrano, S. M., Miralles, D. G., Mcdowell, N., Brodribb, T., Domínguez-castro, F., Leung, R., & Koppa, A. (2022). The uncertain role of rising atmospheric CO_2 on global plant transpiration. *Earth-Science Reviews*, *230*(February), 104055. https://doi.org/10.1016/j.earscirev.2022.104055

Wan, Z. (2019). Collection-6.1 MODIS land surface temperature products users' guide. https://doi.org/10.5067/MODIS/MOD11C3.061

Wielicki, B. A., Barkstrom, B. R., Harrison, E. F., Lee, R. B., Smith, G. L., & Cooper, J. E. (1996). Clouds and the Earth's radiant energy system (CERES): An earth observing system experiment. *Bulletin America Meteorology Social*, *77*(5), 853–868. https://doi.org/10.1175/1520-0477(1996)077<0853:CATERE>2.0.CO;2

Williamson, M. S., Thackeray, C. W., Cox, P. M., Hall, A., Huntingford, C., & Nijsse, F. J. M. M. (2021). Emergent constraints on climate sensitivities. *Reviews of Modern Physics*, *93*(2), 1–39. https://doi.org/10.1103/RevModPhys.93.025004

Wright, M. N., & Ziegler, A. (2017). ranger: A fast Implementation of random forests for high dimensional data in C++ and R. *Journal of Statistical Software*, *77*(1), 1–17. https://doi.org/10.18637/jss.v077.i01

Yin, D., Roderick, M. L., Leech, G., Sun, F., & Huang, Y. (2014). The contribution of reduction in evaporative cooling to higher surface air temperatures during drought. *Geophysical Research Letters*, *41*(22), 7891–7897. https://doi.org/10.1002/2014GL062039

Yuan, K., Zhu, Q., Riley, W. J., Li, F., & Wu, H. (2022). Understanding and reducing the uncertainties of land surface energy flux partitioning within CMIP6 land models. *Agricultural and Forest Meteorology*, *319*, 108920. https://doi.org/10.1016/j.agrformet.2022.108920

Zhang, Y., Narayanappa, D., Ciais, P., Li, W., Goll, D., Vuichard, N., et al. (2022). Evaluating the vegetation–atmosphere coupling strength of ORCHIDEE land surface model (v7266). *Geoscientific Model Development*, *15*(24), 9111–9125. https://doi.org/10.5194/gmd-15-9111-2022